Internal Oscillations of Tropical Mesoscale Convective Disturbances

Bolei Yang[1,2], William R. Boos[2,3], Zhe-Min Tan[4], and Ji Nie[1,5]

1. Laboratory for Climate and Ocean-Atmosphere Studies, Department of Atmospheric and Oceanic Sciences, School of Physics, Peking University, Beijing, China
2. Department of Earth and Planetary Science, University of California, Berkeley, Berkeley, California
3. Climate and Ecosystem Sciences Division, Lawrence Berkeley National Laboratory, Berkeley, California
4. Key Laboratory for Mesoscale Severe Weather, School of Atmospheric Sciences, Nanjing University, Nanjing, China
5. China Meteorological Administration Tornado Key Laboratory, Foshan, China

Corresponding author: Ji Nie
Email: nieji1984@gmail.com

This paper has been accepted by Journal of the atmospheric sciences, https://doi.org/10.1175/ JAS-D-24-0282.

Abstract

In real-world observations, long-lived tropical mesoscale convective disturbances (MCDs) often exhibit quasi-periodic variations in precipitation and cloudiness on time scales of tens of hours. Previous studies suggested that these variations are mainly induced by external forcings such as the diurnal cycle of insolation. However, some studies showed evidence that tropical MCDs can display quasi-periodic behavior even without external forcings. In this study, a suite of idealized convection-permitting simulations is used to examine the evolution of a mesoscale atmospheric column after an initial pulse of heating. It is demonstrated that the heated column not only radiates inertia-gravity waves that perturb its environment, but itself continues to oscillate with consequences for subsequent local convection. By comparing simulations with linear wave theory, it is suggested that this oscillation is an inertia-gravity oscillation. This study indicates that convectively coupled internal oscillations may constitute a fundamental component of the life cycle of observed long-lived tropical MCDs.

1. Introduction

Mesoscale convective disturbances (MCDs) are frequently observed in Earth's tropical regions. These disturbances typically encompass or are associated with systems like mesoscale convective systems, tropical depressions, tropical cyclones (TCs), and monsoon low-pressure systems (LPSs), with sizes ranging from hundreds to thousands of kilometers. These convective systems not only play a crucial role in the water and energy cycles within the tropics, but also significantly impact our social and economic activities (e.g., Nesbitt et al. 2000; Emanuel 2018; Houze 2018). However, the mechanisms driving the evolution of these systems remain incompletely understood.

In real-world observations and numerical simulations, long-lived tropical MCDs often interact with external forcings and demonstrate significant periodicity in precipitation, cloudiness and convective heating. A typical example is the occurrence of large-scale, westward-propagating convective disturbances with periods of approximately 2 days in the equatorial western Pacific (e.g., Takayabu 1994; 1996). Studies indicated that this 2-day period of convection is forced by the propagation of equatorial waves with wavelengths of around 2000 to 4000 km (e.g., Haertel and Johnson 1998; Wheeler et al. 2000; Haertel and Kiladis 2004). Another example is the diurnal cycle of convection over the tropical ocean. In the nighttime, the absence of shortwave heating cools the troposphere, which fosters convection by increasing relative humidity and enhancing convective instability. Conversely, convection is inhibited during the daytime due to strong shortwave heating in the free-troposphere (e.g., Gray and Jacobson 1977; Fingerhut 1978). This diurnal cycle of convection is robust in nearly all types of tropical MCDs, particularly in those with longer lifetimes, such as TCs (e.g.; Browner et al. 1977; Dunion et al. 2014; Wu et al. 2015).

However, in many idealized simulations without external forcing, tropical MCDs also exhibit pronounced quasi-periodic variations. For instance, in many idealized TC genesis simulations, which lack both the diurnal insolation cycle and lateral boundary forcing, significant quasi-periodic pulses of the disturbance can often be seen (e.g., Nolan 2007; Nicholls and Montgomery 2013; Yang and Tan 2020). Some studies suggested that this behavior may be a model artifact resulting from the use of doubly periodic boundary conditions, wherein gravity waves can return to their source and trigger new convection (e.g., Nolan, 2007). Nonetheless, in simulations with very large domains or damping lateral boundary conditions, quasi-periodic variation of the TC disturbances still occurs (e.g., Li et al. 2006; Nicholls 2015). Similarly, quasi-periodic variations can also be seen in idealized simulations of monsoon LPSs (e.g., Diaz and Boos, 2021a, b). These results suggest that the quasi-periodic behavior of tropical MCDs are not solely attributable to external forcing, but may also be internally generated.

The aim of this work is to determine whether a tropical MCD could internally generate quasi-periodic behaviors and, if so, to identify the mechanisms underlying those behaviors. The rest of the paper is organized as follows: Section 2 introduces the simulation details. Section 3 briefly analyzes the internal quasi-periodic behavior in full-physics simulations. Section 4 provides evidence for the critical role of low-level buoyancy in determining the precipitation. Section 5 demonstrates that the inertia-gravity oscillation is responsible for the quasi-periodic behavior of low-level buoyancy and precipitation. Finally, Section 6 offers a discussion and summary.

2. Full-physics simulation design

In this work, we use idealized numerical simulations to investigate the internal oscillations of tropical MCDs. The numerical model employed is the WRF version 4.6.0 (Skamarock et al., 2019). The model domain extends to an altitude of 27 km, with the upper third consisting of a sponge layer (Klemp and Lilly 1978). There are 50 vertical levels, with 10 levels located below 1 km height. The initial sounding is derived from Jordan (1958), which is a typical tropical sounding commonly used in simulations.

The simulations cover a horizontal domain size of 1800 km × 1800 km, with a horizontal resolution of 3 km. To rule out the effects of gravity waves propagating back to their sources, the best way should be using open lateral boundary conditions so that gravity waves can radiate out of the domain. However, in our preliminary simulations (not shown), adopting open lateral boundary condition leads to a drastic drying of the domain, with the domain-mean moisture content decreasing by 40% in the first 3 days. This is probably because open boundary condition allows water vapor to escape out of the domain. Therefore, we still use doubly periodic lateral boundary condition, but add a sponge layer at the lateral boundaries of the domain (e.g., Li et al., 2006). This sponge layer is 180 km wide at the lateral boundaries, with the diffusion coefficient set to 1000 times the model's predicted value (based on a 1.5-order TKE closure). The simulations maintain a fixed sea surface temperature SST of 302.15 K and a constant solar radiation of 350 W m^{-2} with no diurnal cycle. The Thompson microphysics scheme (Thompson et al., 2004) and the RRTMG radiation scheme (Iacono et al. 2008) are implemented in the simulations. The boundary layer (BL) scheme is YSU, coupled with the revised Monin–Obukhov surface-layer scheme (Hong et al. 2006).

All simulations initiate with a moist anomaly characterized by enhanced humidity at the center of the domain. This moist anomaly has a radius of 150 km and a height of 3 km (starting at the surface), with the water vapor mixing ratio inside set to be 110% (horizontally uniform) of the initial sounding value. We conduct three simulations with Coriolis parameter set to 10^{-4} s^{-1} (CTLF10), 5×10^{-5} s^{-1} (CTLF05) and 0 s^{-1} (CTLF0), respectively (Table 1). All the simulations are run for 72 hours, and results are output every 2 hours. In the following analysis, we will mainly focus on the results in CTLF10, and the results in the other two experiments will be briefly compared.

Table 1 Descriptions of full-physics experiments.

Name	**Description**
CTLF10	An 1800 km×1800 km full-physics simulation with Coriolis parameter set to be 1×10^{-4} s^{-1}. The lateral boundary condition is double periodic, with a damping layer of 180 km wide.
CTLF05	As CTLF10, with Coriolis parameter set to be 5×10^{-5} s^{-1}.
CTLF0	As CTLF10, without Coriolis force.

3. Internal oscillation of tropical MCDs

The time series of the precipitation rate in the disturbed region (defined to be the inner 150 km radii of the disturbance) of the three simulations are shown in Fig. 1a. All three simulations exhibit a significant quasi-periodic pulsing in precipitation. The range of the quasi-periodic precipitation variations is approximately 0.08 to 0.15 mm h^{-1}, representing about 30% (CTLF10) to 50% (CTLF0) of the mean precipitation. In contrast, the precipitation pulsing observed in real-world Atlantic tropical cyclones (TCs) is approximately 0.3 mm h^{-1} (Wu et al., 2015), which constitutes roughly 10% of the mean precipitation. Therefore, the pulsing observed in the 'CTL' simulations may be larger than real-world analogues. The pulsing periods in CTLF10, CTLF05 and CTLF0 are around 15 hours, 18 hours and 28 hours (the period is defined as the time lag between the first and the last precipitation peaks divided by the number of cycles), respectively, indicating a noticeable increase in the period as the Coriolis parameter decreases. We further conduct sensitivity simulations based on CTLF10 to examine the influence of domain size on the pulsing period. As shown in Fig. A1, variations in domain size do not have a discernible effect on the pulsing period, which suggests that the gravity wave return mechanism, as proposed in previous studies (e.g., Nolan, 2007), is unlikely to be responsible for the observed pulsing. The water vapor path (WVP) in the disturbance region also shows a significant pulsing signal, which is almost in phase with the precipitation (Fig. 1b).

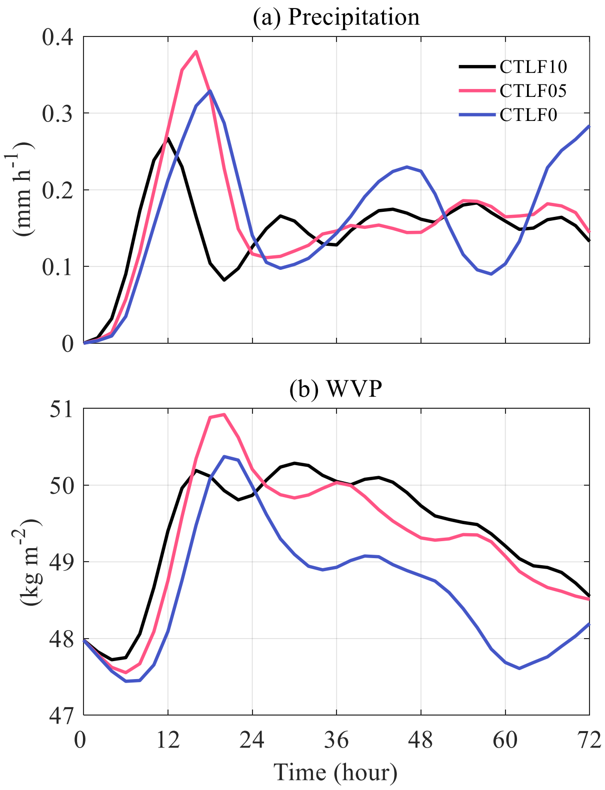

Fig.1 Time series of (a) precipitation rate (mm h^{-1}) and (b) water vapor path (kg m^{-2}) over the inner 150 km radii of the disturbance in CTLF10 (black), CTLF05 (red), and CTLF0 (blue).

To confirm that this quasi-periodic pulsing is physically meaningful rather than a result of model noise, we present plane views of WVP from 22 h to 52 h in CTLF10 (Fig. 2). In Fig. 2, the WVP shows clear variations, mainly confined to the initially disturbed area. The WVP has an increasing trend from 22-28 h and 38-44 h, and a decreasing trend from 30-36h and 46-52h, consistent with the variation of WVP shown in Fig. 1b.

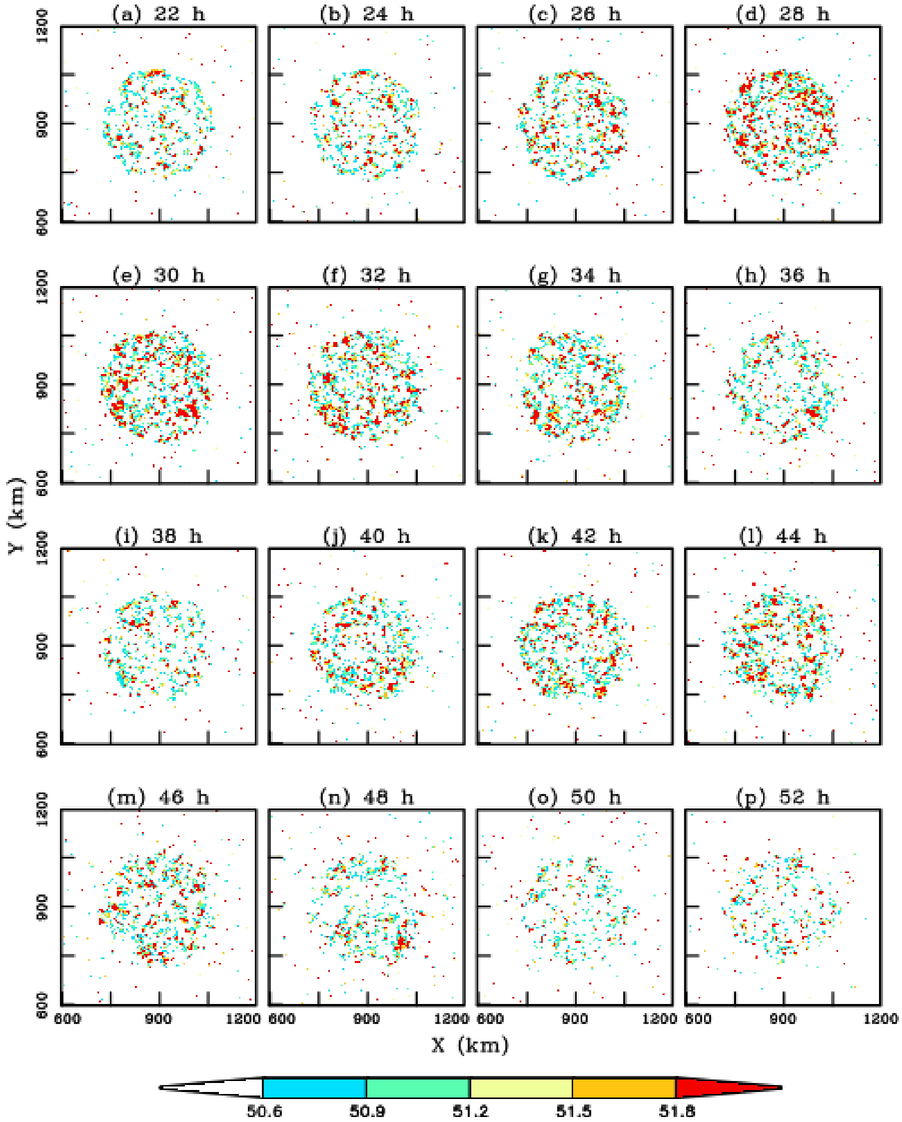

Fig. 2 Plane views of water vapor path (kg m^{-2}) from 22 h to 52 h in CTLF10.

We also present time-height plots of vertical velocity and diabatic heating averaged over the disturbed area during the whole simulation. Given that the disturbed columns exhibit a systematic warming trend at upper levels and an elevated convective top throughout the entire 3-day simulation period (Fig. A2), we use a moving average method to filter out variations longer than 30 hours. The filtered variables exhibit clear periodic features in the central column of the domain (where the disturbance was initiated with the initial moisture anomaly) across all simulations (Fig. 3). Based on the results after filtering, we define periods with positive mass-weighted vertical integrated vertical velocity as the convectively active stages, and those with negative column-integrated vertical velocity as the convectively suppressed stages. In CTLF10, the first active stage occurs from 6 h to 16 h. The mean latent heating profile shows a vertical half-wavenumber structure in the free-troposphere (above the BL top). Unlike the first baroclinic mode observed in real-world scenarios (e.g., Haertel and Kiladis 2004; Houze, 2018), the latent heating here exhibits a bottom-heavy structure, with its maximum around 1 km altitude (Fig. 4a). The first suppressed stage occurs from 16 h to 24 h, during which latent heating is significantly weaker compared to the developing stage. In this stage, the heating displays a more complicated vertical structure, characterized by heating from the BL top to 4.4 km, cooling from 4.4 km to 5.8 km, and additional heating from 5.8 to 10 km height (Fig. 4a). Although the peak heating occurs in the upper troposphere, the vertical structure in the suppressed stage does not clearly resemble the stratiform (wavenumber-one) structure seen in previous studies (e.g., Haertel and Kiladis 2004; Houze, 2018).

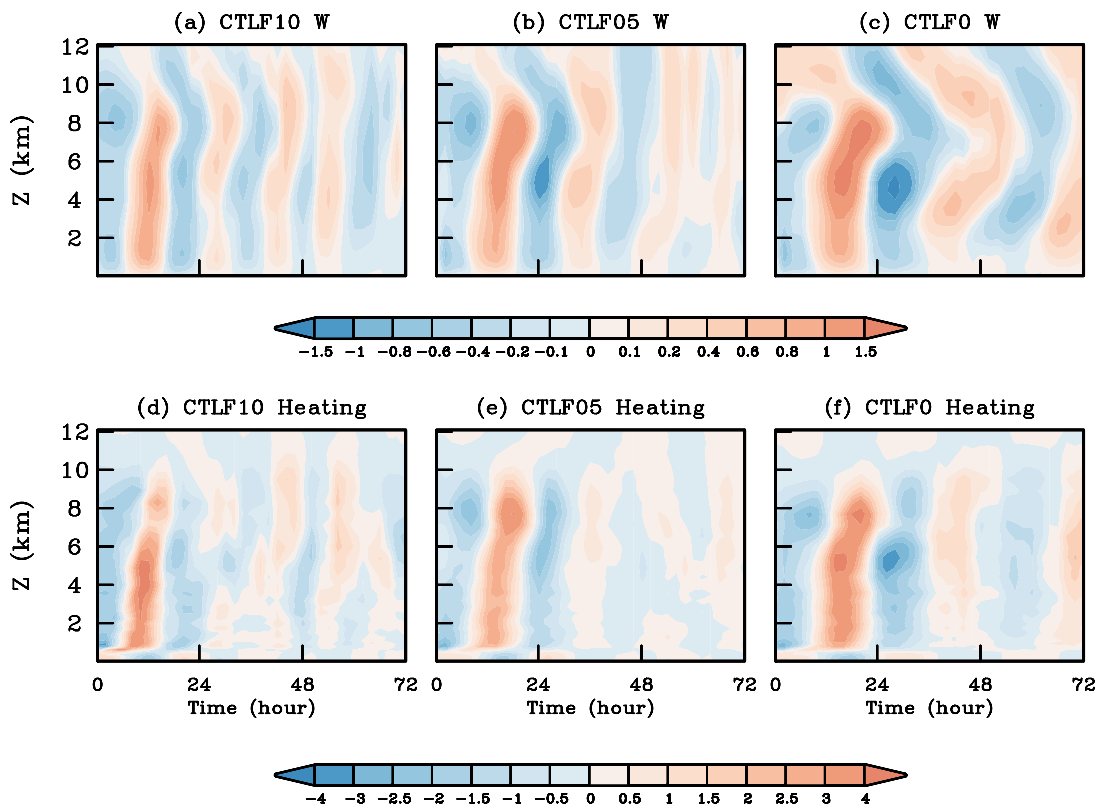

Fig. 3 Time-height plot of (a) vertical velocity ($\mathrm{cm\ s^{-1}}$) and (d) diabatic heating ($\mathrm{K\ day^{-1}}$) in CTLF10, with signals longer than 30 hours filtered out. All the variables are averaged in the inner 150 km radii of the domain. (b), (e) and (c), (f) are for CTLF05 and CTLF0, respectively.

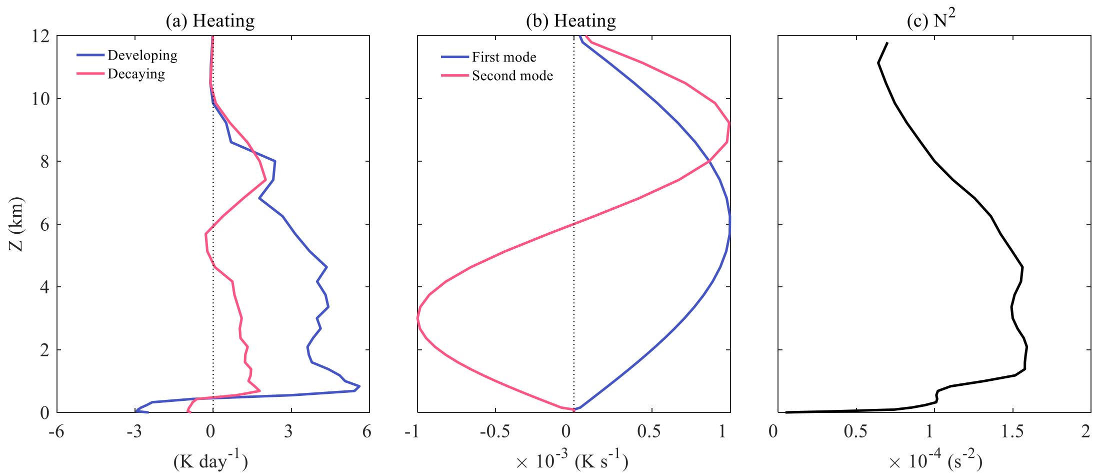

Fig. 4 Vertical profiles of (a) the latent heating profiles averaged in the first active (blue) and suppressed (red) stage of CTLF10, (b) the first (blue) and second (red) diabatic

heating mode (K s^{-1}) used in the dry simulations, and (c) the N^2 (s^{-2}) averaged in the initial 2 hours over the disturbed area.

In this first suppressed stage, subsidence occurs in the lower levels of the disturbed column, extending from 6 km down to the surface (Fig. A2a). This downward motion and the associated drying (between hours 16-24; Figs. 1b & 3) might be expected to inhibit subsequent convection at the same location (e.g., Houze, 1982; Houze, 2018). However, deep convection is reinvigorated after 24 hours, and the initially disturbed column repeats this cycle of active and suppressed convection over the next several days (Figs. 1 & 3). A similar pattern is seen in CTLF05 and CTLF0, although the periods of the cycles differ (Figs. 1 & 3).

The occurrence of quasi-periodic convection raises two questions: What mechanisms facilitate the recovery of deep convection following the downward motion in the disturbed air column? Additionally, what determines the period of the cycle? We will address these questions in the next two sections.

4. Convective recovery: the role of low-level buoyancy

To understand the recovery of convection after the suppressed stage in the disturbed column, we need to understand the evolution of the variables that determine convective activity. Previous studies have demonstrated that low-level buoyancy plays a crucial role in determining precipitation in tropical MCDs (e.g., Ahmed and Neelin 2018; Ahmed et al. 2020). Following Ahmed et al. (2020), the low-level buoyancy of an entraining convective plume can be approximated as:

$$B_{low} = g\left(w_1 \frac{\theta_{eBL} - \theta^*_{eL}}{\theta^*_{eL}} - w_2 \frac{\theta^*_{eL} - \theta_{eL}}{\theta^*_{eL}}\right), \qquad (1)$$

in which θ_{eBL} is the BL averaged θ_e, θ_{eL} is the θ_e averaged in the lower free-troposphere, and θ^*_{eL} is the saturation θ_e in the lower free-troposphere. The first term on the right-hand side of Eq. (1) can be interpreted as an approximate measure of the undilute plume buoyancy based on BL properties and lower free-tropospheric temperature, and the second term measures the influence of lower free-tropospheric subsaturation on the plume via entrainment. The coefficients w_1 and w_2 are the weights of the two processes, which can be expressed as:

$$w_1 = \frac{\Delta p_{BL}}{\Delta p_L} \ln\left(\frac{\Delta p_{BL} + \Delta p_L}{\Delta p_{BL}}\right),$$

$$w_2 = 1 - w_1.$$

In this study, the BL and the low-level troposphere are defined as the layer below 900 hPa and the layer between 900 hPa and 500 hPa, respectively. With this definition, w_1 and w_2 are 0.4 and 0.6, respectively, but we follow parts of Ahmed et al. (2020) and henceforth use $w_1 = w_2 = 0.5$ to estimate the low-level buoyancy. All vertically averaged variables in Eq. (1) are density weighted.

The time evolution of B_{low} in the 'CTL' simulations is shown in Fig. 5. Except for the last 12 hours in 'CTLF05', the evolution of B_{low} is generally in phase and strongly correlated with precipitation in the disturbance region in all three simulations after 12 h. For comparison, plane views of B_{low} from 22 to 54 h in CTLF10 are also presented in Fig. 6. It is evident that the most significant variations in B_{low} occur in the central column that was initially disturbed, which generally retains its size, shape, and location throughout the simulation. B_{low} shows an increasing trend from 22-28 h and 38-44 h, and a decreasing trend from 30-36h and 46-52h, consistent with the variations of precipitation and B_{low} shown in Fig. 5a.

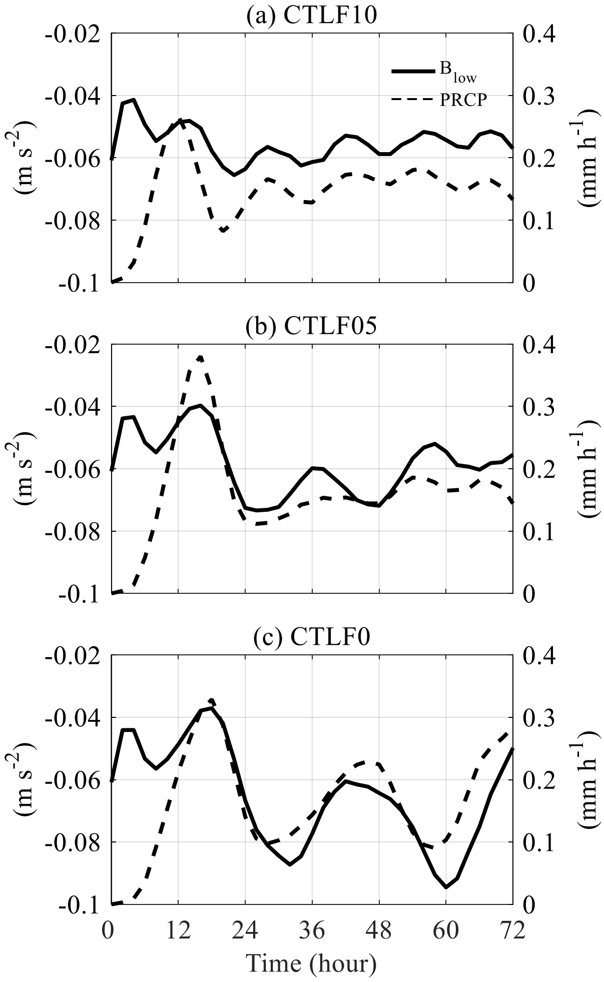

Fig. 5 Time series of low-level buoyancy (solid, m s^{-2}) and precipitation rate (dashed, $\mathrm{mm\ h^{-1}}$) over the inner $150\ \mathrm{km}$ radii of the disturbance in (a) CTLF10, (b) CTLF05, and (c) CTLF0.

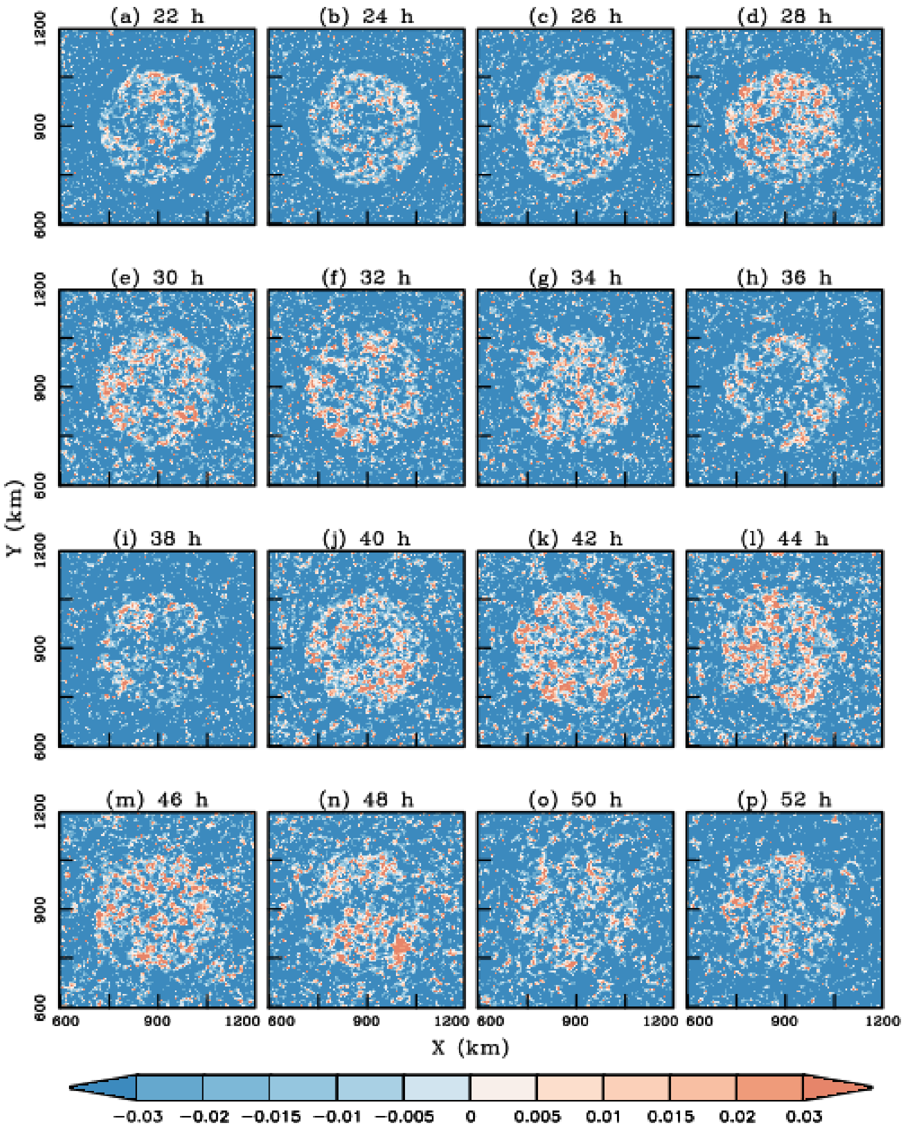

Fig. 6 Plan views of B_{low} (m s^{-2}) from 22 h to 52 h in CTLF10. We add a constant value of 0.05 to make B_{low} in the disturbance region around 0.

To further investigate whether the evolution of B_{low} quantitatively reflects precipitation changes, we reference the P- B_{low} relationship established in Ahmed et al. (2020, their Fig. 2) and find that sensitivity of a=5 (mm h^{-1}) (m s^{-2})$^{-1}$ provides an approximate fit in our simulations[1]. Here, we calculate the precipitation anomaly using

[1] Ahmed et al. (2020) found larger sensitivities of precipitation to buoyancy (a=20 (mm h^{-1}) (m s^{-2})$^{-1}$) than what we use here, but those were for positive buoyancies. In our simulations the precipitation occurs at weakly negative buoyancies, which is consistent with the smaller sensitivity

the variation of B_{low} in CTLF10, and compare it with the temporal precipitation anomaly from 0-72 h in CTLF10. As shown in Fig. 7, the temporal precipitation anomalies estimated from buoyancy variations are a close match to the explicitly simulated precipitation. This further validates the use of low-level buoyancy as a means of quantitatively understanding the evolution of convection in the disturbed column. Nonetheless, it is important to recognize that while B_{low} correlates well with precipitation, the absolute values do not always align. For instance, at 44 hours, B_{low} in CTLF0 is lower than in CTLF10, yet the precipitation in CTLF0 is greater (Fig. 5).

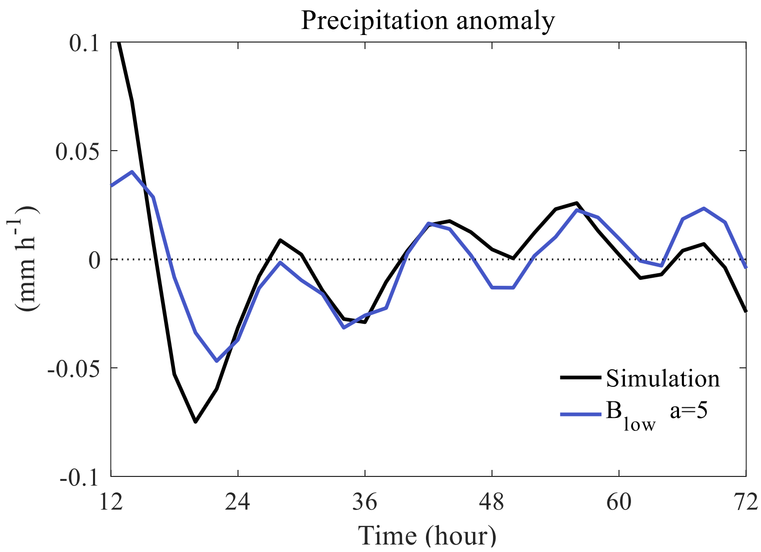

Fig. 7 Time series of temporal precipitation anomaly (mm h^{-1}) from 12-72 h in the disturbance in CTLF10 (black) and the precipitation anomaly estimated with low-level buoyancy (blue).

The above analysis indicates that, following the decay of the initial pulse of precipitating convection, the recovery of low-level buoyancy is critical to the recovery of deep convection and precipitation. According to equation (1), there are three factors controlling the low-level buoyancy: the BL θ_e, the temperature in the lower free-

we use here.

troposphere, and water vapor mixing ratio (q_v) in the lower free-troposphere. A higher BL θ_e, a larger lower free-tropospheric humidity, or a colder lower free-tropospheric temperature produce an increased B_{low}. To identify which factor dominates the evolution of B_{low}, we calculate B_{low} in CTLF10 again but substitute the BL θ_e with its temporal mean from 0-72 h. Fixing the BL θ_e in Eq. (1) introduces a systematic trend in B_{low} for the duration of the simulation, but retains significant pulsing in B_{low} (Fig. 8a). However, when the temperature and moisture variation in the lower free-troposphere is removed using the same method, the pulsing signal in B_{low} greatly diminishes (Fig. 8a). This indicates that for B_{low} to recover, it is the lower free-troposphere that matters most.

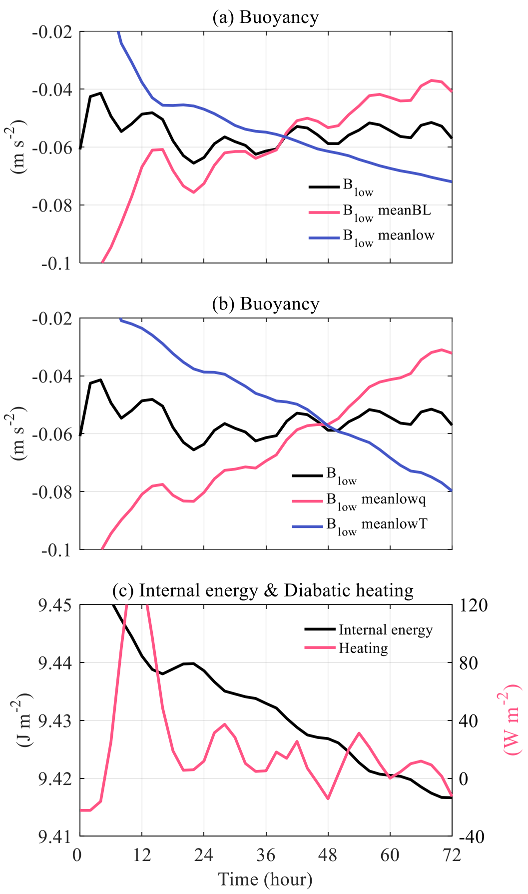

Fig. 8 (a) Time series of the original B_{low} (m s^{-2}) in CTLF10 (black), B_{low} calculated

with a 0-72 h temporal mean BL variables (B_{low}_meanBL, red), and B_{low} calculated with 0-72 h temporal mean lower free-tropospheric variables (B_{low}_meanlow, blue) in CTLF10. (b) Time series of the original B_{low} in CTLF10 (black), B_{low} calculated with a 0-72 h temporal mean lower free-troposphere q_v (B_{low}_meanlowq, red), and B_{low} calculated with a 0-72 h temporal mean lower free-troposphere temperature (B_{low}_meanlowT, blue) in CTLF10. (c) Time series of lower free-tropospheric mass-weighted internal energy (black, J m^{-2}) and diabatic heating (red, W cm^{-2}) in CTLF10.

We further investigate which characteristics in the lower free-troposphere are most significant in influencing the pulsing of B_{low}. We recalculated B_{low} in CTLF10 by substituting the free-tropospheric temperature and water vapor with their temporal means from 0 to 72 hours. The results indicate that the pulsing of B_{low} is controlled mostly by the temperature in the lower free-troposphere (Fig. 8b; the variance of the detrended B_{low}_meanlowT line in Fig. 8b is about one-third the variance of the detrended B_{low}_meanlowq line). This suggests that the variation of low-level temperature plays a primary role in the variation of B_{low}, and in turn, the variation in precipitation.

In this section, we demonstrated that the oscillation of deep convection and precipitation could be explained by the oscillation of low-level buoyancy, which is primarily influenced by variations in the lower free-tropospheric temperature. However, the mechanisms causing these temperature variations remain unclear. Previous theoretical studies have argued that diabatic cooling in the lower free-troposphere by stratiform convection can produce a decrease of lower free-tropospheric temperature following deep convective heating (e.g., Mapes 2000; Kuang 2008b). However, in our simulations, the diabatic cooling caused by stratiform precipitation is relatively weak. In some cases, there is even no discernible diabatic cooling in the lower free-troposphere (e.g., CTLF05, Fig. A2e). Furthermore, Fig. 8c generally shows an out-of-phase relationship (in a signal that is admittedly noisy) between temperature anomalies and diabatic heating anomalies, with multiple instances of positive temperature tendency anomalies occurring while diabatic heating anomalies are negative. This suggests that the decrease of lower free-tropospheric temperature during the oscillation is not directly caused by diabatic cooling of a stratiform heating structure. In the following section, we will explore the occurrence of cooling in the lower free-troposphere and the recovery of buoyancy from the perspective of adiabatic processes.

5. Recovery of Buoyancy: an inertia-gravity oscillation

In this section, we conduct a series of simulations without latent heating (or cooling), termed 'Dry', to investigate the recovery of buoyancy in tropical MCDs after the suppressed stage (Table 2). These simulations have a domain size of 3000 km × 3000 km with open lateral boundary conditions. Additionally, there is no radiation or microphysics parameterization. The other settings remain consistent with the 'CTL' series.

Table 2 Descriptions of dry experiments.

Name	Description
Dry_Active	A 3000 km×3000 km simulation forced with the heating profile averaged in the active stage of CTLF10. There is no microphysics or radiation parameterization, and the open lateral boundary condition is used. The other settings are as in CTLF10.
Dry_Suppressed	As in Dry_Active, but forced with the heating profile averaged in the suppressed stage.
Dry2_F10	As in Dry_suppressed, but forced with the stratiform heating profile shown in Fig. 6b.
Dry2_F05	As in Dry2_F10, but with Coriolis parameter set to be 5×10^{-5} s^{-1}.
Dry2_F0	As in Dry2_F10, but without Coriolis forcing.
Dry1_F10	As in Dry2_F10, but forced with a deep convective heating profile shown in Fig. 6b.
Dry1_F05	As in Dry1_F10, but with Coriolis parameter set to be 5×10^{-5} s^{-1}.
Dry1_F0	As in Dry1_F10, but without Coriolis force.

We first test the response of the disturbed column to heating in the convectively active (Dry_active) and suppressed (Dry_ suppressed) stage, as defined in section 3 (Fig. 5a). In all the dry simulations, the imposed diabatic heating is maintained for two hours, followed by an additional 46 hours of simulation. In both Dry_active and Dry_ suppressed, the diabatic heating produces subsequent damped oscillations of multiple variables including B_{low} (Figs. 9 and 10a).

The purpose of the full-physics 'CTL' simulations is to show that, even when initiated from a simple moist bubble, the resulting MCD can show a pulsing signal. However, the heating profiles shown in Fig. 4 are highly atypical of real-world conditions. In real-world observations, tropical MCDs usually exhibit a half-wavenumber vertical structure during the development of deep convection, and a wavenumber-one vertical structure during the decay of deep convection (e.g., Haertel and Kiladis 2004; Houze 2018). To better understand the mechanism of the oscillation and to draw closer connections to real-world scenarios, we conduct a second set of dry simulations forced by a vertical wavenumber-one heating structure ('Dry2'; Table 1).

The heating structure in the 'Dry2' simulations is given as follows:

$$Q(r,z) = \begin{cases} Q_0 \sin(2\pi z/H - \pi)\cos(\pi r/2R) & (z < H \; and \; r < R) \\ 0 & (z \geq H \; or \; r \geq R) \end{cases} \quad (2)$$

In Eq. (2), r and z represent radius and height, respectively. H and R are the maximum height and radius of the heating, which are 12 km and 150 km, respectively. Q_0 is the magnitude of the heating, which is set to be 0.001 K s^{-1}. This heating has a typical second baroclinic mode (stratiform heating profile) in the vertical direction (Fig. 4b), which also decays sinusoidally with radius. The magnitude of the heating is chosen to be roughly 20 times stronger than the diabatic heating in the developing phase of the full-physics model (Fig. 4a) to both better match diabatic heating values in observed real-world synoptic systems and obtain a better signal-to-noise ratio (simulations using a weaker forcing with magnitude of 1 x 10^{-4} K s^{-1} produces qualitatively similar results).

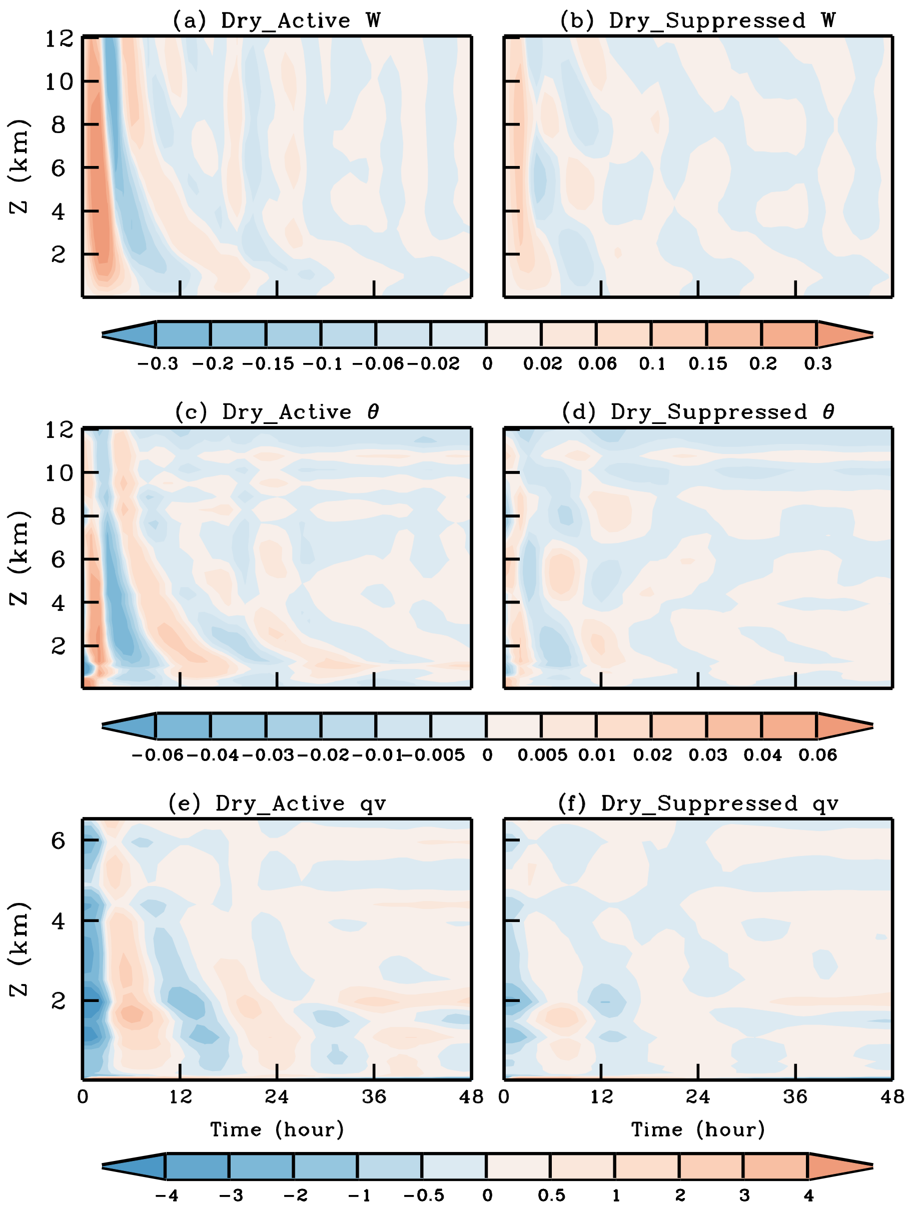

Fig. 9 The time-height plot of (a) vertical velocity (cm s^{-1}), (c) temporal potential temperature anomaly (K), and (e) temporal q_v anomaly (g kg^{-1}), all averaged in the inner 150 km radii of the central column in Dry_Active. (b), (d) and (f) are the corresponding variables for Dry_ Suppressed.

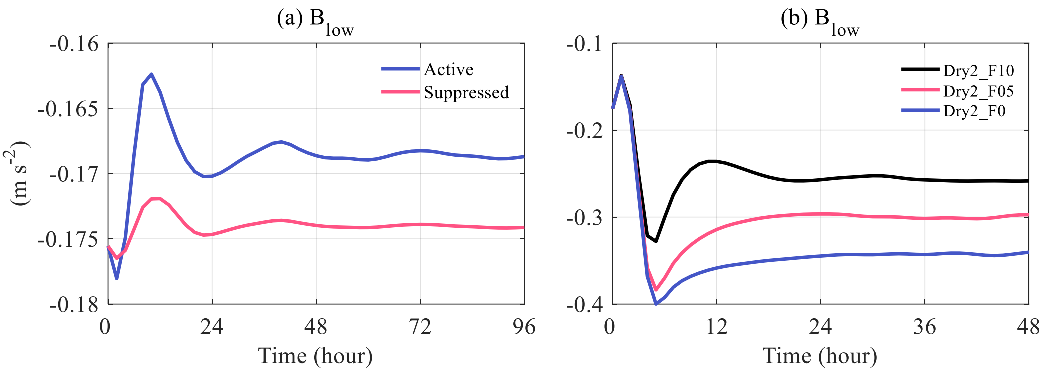

Fig. 10 (a) Time series of B_{low} (m s^{-2}) in Dry_Active (blue) and Dry_ Suppressed (red). (b) Time series of B_{low} (m s^{-2}) in Dry2_F10 (black), Dry2_F05 (red), and Dry2_F0 (blue).

The immediate response of the air column in Dry2_F10 to the heating is characterized by upward motion above 6 km and downward motion below 6 km (Fig. 10a). Although these vertical motions may induce adiabatic cooling at upper levels and warming at lower levels, they are insufficient to offset the diabatic heating and cooling over such a short time frame. Consequently, warm and cold anomalies develop at 9 km and 3 km, respectively, during the initial hours (Fig. 11d). Additionally, the vertical motion redistributes water vapor, with subsidence over the first several hours inducing a drying tendency at lower levels. Note that both potential temperature and q_v exhibit stronger vertical variations than temporal variations. To better isolate the temporal oscillations of interest, we remove the time-mean vertical profile from both fields in Fig. 11, so a secular drying trend over the course of the simulation yields a moist anomaly during the initial few hours that decays in response to the subsidence.

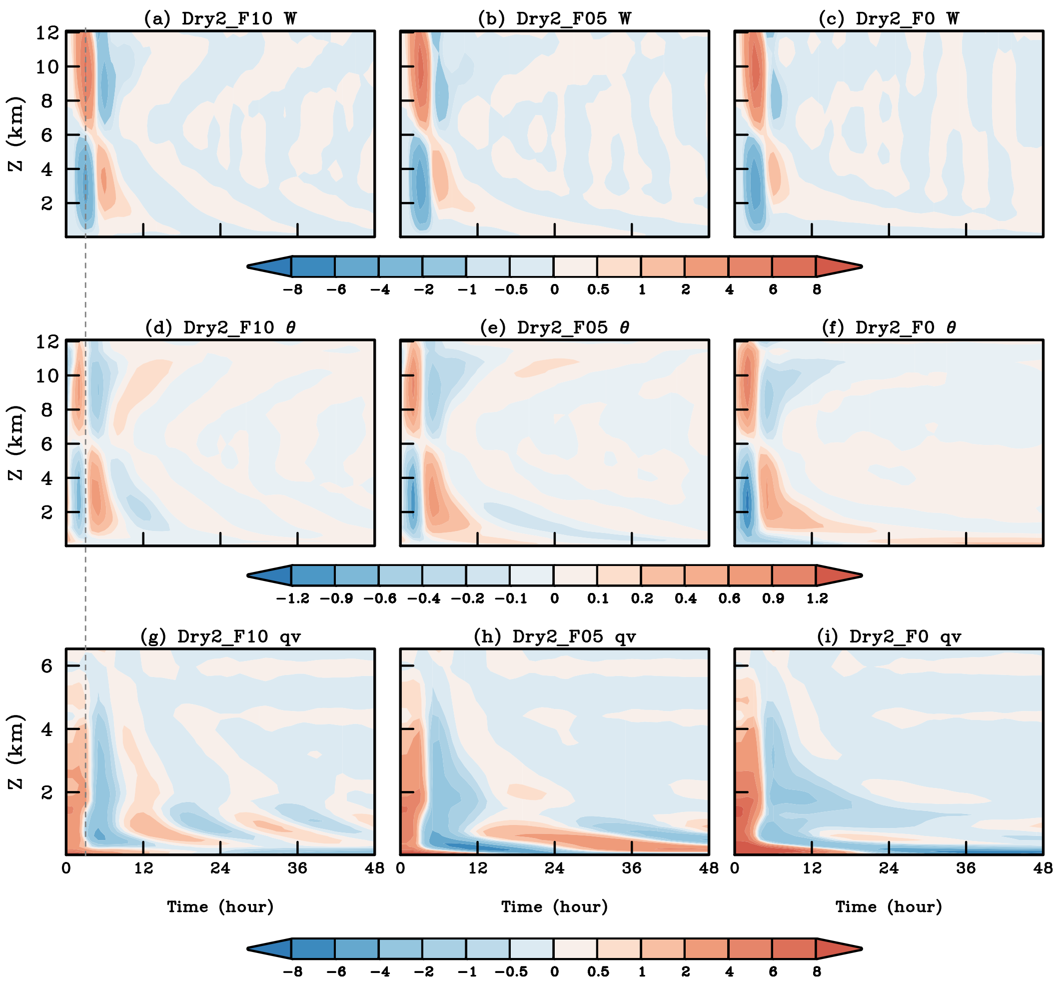

Fig. 11 The time-height plot of (a) vertical velocity (cm s^{-1}), (d) temporal potential temperature anomaly (K), and (g) temporal q_v anomaly (g kg^{-1}), all averaged in the inner 150 km radii of the domain in Dry2_F10. (b), (e), (h) and (c), (f), (i) are for Dry2_F05 and Dry2_F0, respectively. The vertical dashed line marks the moment that the vertical velocity in the lower free-troposphere reaches the first minimum, indicating that the temperature and q_v anomaly is 1/4 period behind the vertical velocity.

Although the diabatic heating ceases after 2 hours, the response of vertical motion persists for a significantly longer duration. The evolution of temperature and q_v lags the vertical velocity by one-fourth of the oscillation period, suggesting that vertical motion is the driving force behind the changes in temperature and q_v. The subsidence in the lower free-troposphere further results in warming and drying at lower levels, which decreases low-level buoyancy that would be expected to suppress convection in a simulation with latent heating (Fig. 10b). However, the vertical motion reverses 6 hours after model initialization (4 hours after the cessation of the diabatic forcing), resulting in a cooler and moister lower troposphere that enhances B_{low} (Fig. 10b). In fact, the vertical motion undergoes periodic sign changes, leading to oscillations in temperature and q_v (Figs. 11a, d, & g), and, in turn, B_{low} (Fig. 10b). In Dry2_F05 and Dry2_F0, we also find similar oscillations (Figs. 10b & 11). The oscillation period increases as the Coriolis parameter decreases, consistent with the results of the full-physics simulations (Fig. 1). It is important to note that in all the dry simulations, the oscillation period varies with altitude (Fig. 11), characterized by shorter periods throughout most of the troposphere and longer periods in the upper troposphere and the lowest kilometer (here the period is defined as the time between the first two same-signed vertical velocity extrema). This vertical structure of the period also corresponds to an increase in vertical wavenumber over time (Fig. 11).

We have shown that in dry simulations, an air column perturbed by a stratiform heating profile exhibits internal damped oscillations, which alter low-level buoyancy in ways that would be expected to support oscillations of precipitating convection if condensation occurred. Given that the simulations are conducted on an f-plane within a stratified atmosphere, these oscillations are likely inertia-gravity oscillations. An air column being disturbed usually serves as a wave source, which excites waves that are characterized by specific spatial structures of dynamical and thermodynamic variables. To confirm the inertia-gravity nature of the oscillation, we will now study the property of the waves triggered by the oscillation and compare the characteristics with linear inertia-gravity wave theory.

The radius-height structures of several key variables outside the disturbance region in Dry2_F10, as shown in Fig. 12, indicate an outward propagating wave signal. The first wave front at 10 h exhibits subsidence at upper levels and ascent at lower levels at radii between 400-500 km, and consists of an outward-propagating structure with respective warm and cold anomalies one-fourth of a wavelength behind the vertical motion (Figs. 10a, d & g). This structure aligns with findings from previous studies (e.g., Nicholls et al. 1991; Mapes 1993).

In a linear inertia-gravity wave, when a cold anomaly is situated above a warm anomaly, ascent and outward radial velocity anomalies should exist between these temperature anomalies (e.g., Fig. 5.12 of Holton and Hakim 2012). The left and middle columns in Fig. 12 illustrate that the relationships between temperature and vertical and radial velocity are consistent with this theoretical expectation. Furthermore, theory predicts that tangential velocity maxima should occur where the radial velocity changes sign. As depicted in the right column of Fig. 12, a similar phase relationship is seen in the Dry2_F10 simulation. The similarity of the wave structure with linear theory reinforces the conclusion that the oscillations produced by the initial diabatic forcing in the dry simulations are inertia-gravity oscillations

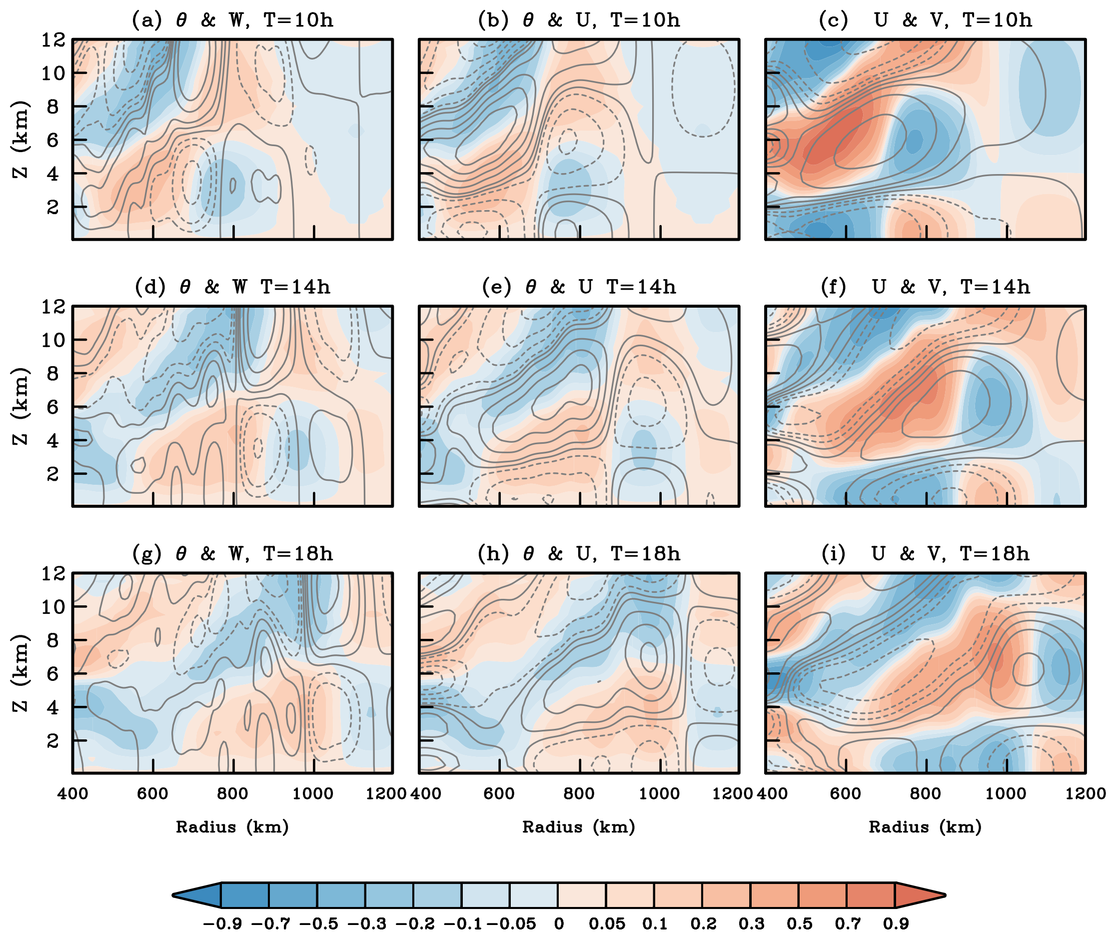

Fig. 12 Radius-height plots of azimuthal-mean (a) horizontal potential temperature anomaly (K, shading) and vertical velocity (contours at -3, -2, -1, -0.5, 0, 0.5, 1, 2 and

3 cm s^{-1}, with solid lines indicating non-negative values and dashed lines indicating negative values), (b) horizontal potential temperature anomaly (K, shading) and radial velocity (contours at 0.9, -0.7, -0.5, -0.3, -0.1, 0, 0.1, 0.3, 0.5, 0.7 and 0.9 m s^{-1}), and (c) radial velocity (cm s^{-1}, shading) and tangential velocity (contours at -0.6, -0.4, -0.2, -0.1, -0.05, 0, 0.05, 0.1, 0.2, 0.4 and 0.6 m s^{-1}). The upper, middle and lower panel are for 10 h, 14 h and 18 h in Dry2_F10, respectively.

For comparison, we present radius-height plots of the same variables from the full-physics simulation CTLF10 (Fig. 13). Due to a systematic warming tendency above 7 km, which may obscure the wave signal, we focus only on the structures below 6 km. In CTLF10, diabatic heating does not have the simple, idealized vertical structure imposed in the dry simulations, so the wave structures are not as clearly defined as those in the dry simulations. Nevertheless, several dominant features of inertia-gravity waves remain evident. For instance, downward motion (dashed lines in Figs. 13a, d & g) consistently precedes the warm anomaly (red shading in Fig. 13a, d & g), the phase lines separating cold and warm anomalies align with peak radial velocity anomalies (Figs. 13b, e & h), and the tangential velocity maxima correspond to points where the radial velocity changes sign (Fig. 13i). These features suggest that even in full-physics simulations, the oscillation generally retains its inertia-gravity characteristics.

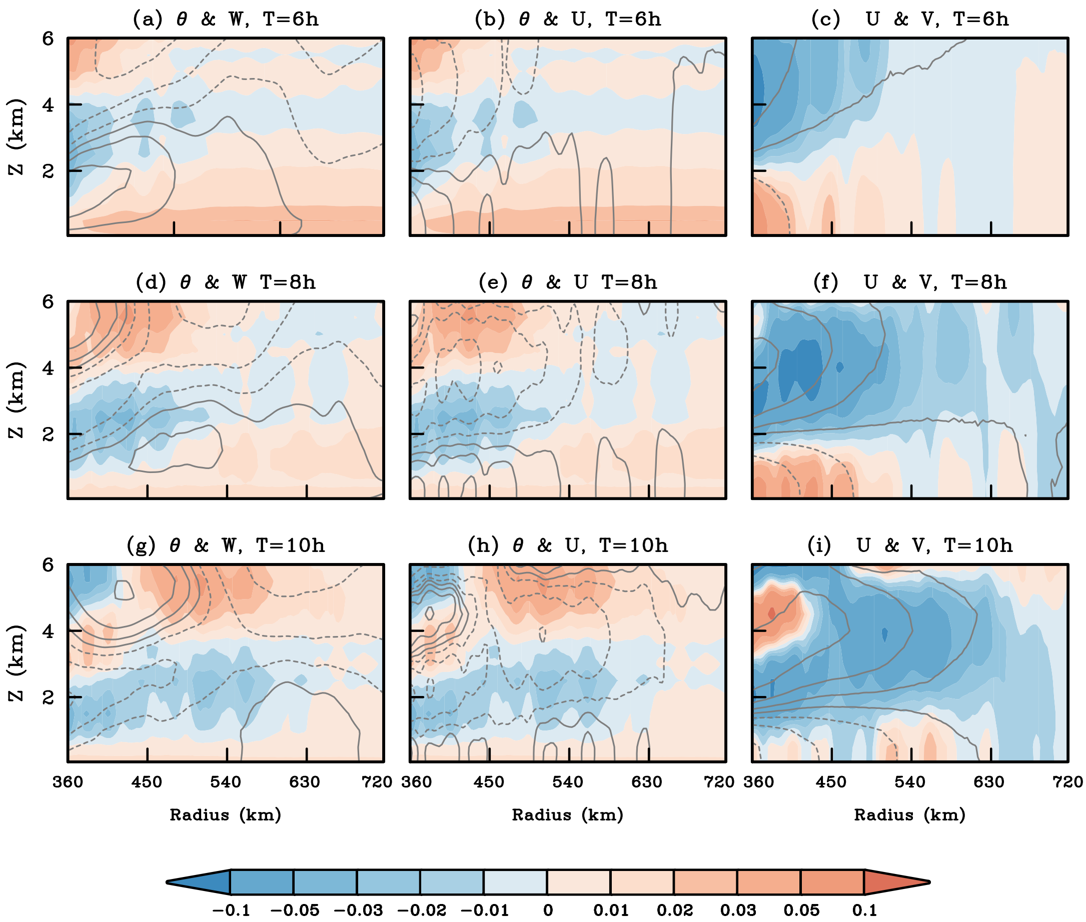

Fig. 13 As in Fig.12, but for CTLF10 at 6 h (upper) 8 h (middle) and 10 h (lower).

While the structure of the wave aligns with inertia-gravity wave theory, more quantitative evidence would come from consistency in the dispersion relationship. According to linear inertia-gravity wave theory,

$$\nu^2 = f^2 + N^2(k^2 + l^2)m^{-2} \quad (3)$$

In Eq. (3), ν is the frequency of the oscillation, f is the Coriolis parameter and N^2 is the buoyancy frequency. k and l are wavenumbers in the x and y directions, respectively, and k^2+l^2 is thus the square of the wavenumber in the radial direction. m is the wavenumber in the vertical direction.

Since we have applied a stratiform heating structure in the disturbance as shown in Fig. 4b, the wavelength in the vertical direction should be 12 km. Potential temperature, vertical motion, and radial velocity exhibit a radial wavelength of around 600 km (Fig. 12), consistent with a linear response to the forcing which has that same wavelength (the diameter of the impose heating is 300 km, so the wavelength trigger by the heating should be 600 km). However, the tangential velocity displays a slightly longer wavelength (Figs. 12f & h), so we use a general wavelength of 750 km. Together with the profile of N^2 averaged in the first 2 hours over the disturbed area (Fig. 4c), we can estimate the oscillation period using Eq. (3). The estimated oscillation period is similar to the period simulated in Dry2_F10 (Fig. 14) and exhibits slightly larger values in the upper troposphere and substantially larger values just above the surface, due to smaller values of N^2 at both upper and lower altitudes. Since the horizontal wavelengths in Dry2_F05 and Dry2_F0 are slightly longer compared to those in Dry2_F10 (Fig. 15), we estimate the general wavelengths in Dry2_F05 and Dry2_F10 to be 900 km and 1050 km, respectively, and the estimated periods are also consistent with those observed in the dry simulations (Fig. 14).

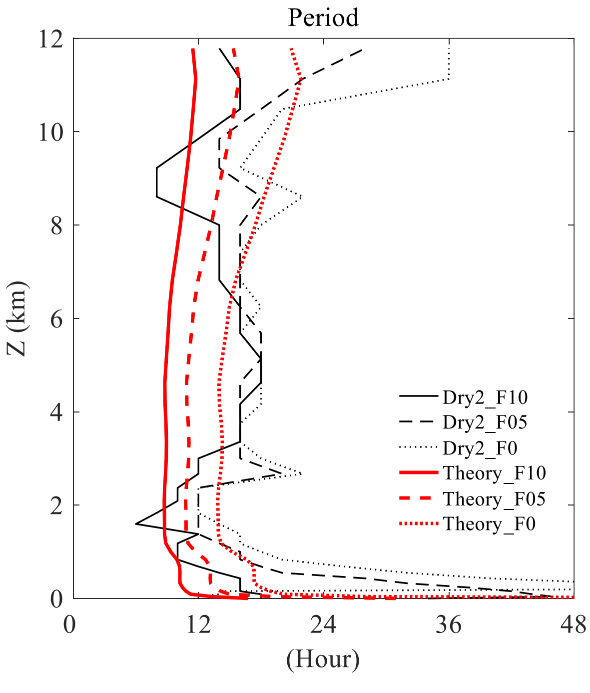

Fig. 14 Vertical profiles of period (in hours) in Dry2_F10 (black solid), Dry2_F05 (black dashed) and Dry2_F0 (black dotted). Red lines are their counterparts estimated by the linear theory.

From the dispersion relationship, we can further infer the phase speed of the wave. The phase speed is written as:

$$c = v\Big/\sqrt{k^2+l^2} \quad (4)$$

We substituted the respective periods and wavelength of Dry2_F10, Dry2_F05, and Dry2_F0 at a height of 3 km (10, 15, and 18 hours, respectively, as shown in Fig. 14) into Eq. (4). This yielded theoretical phase speeds of 20.8 m/s, 16.7 m/s, and 16.2 m/s, respectively. As illustrated in Figs. 15a-c, the phase speeds of the first wave front in Dry2_F10, Dry2_F05, and Dry2_F0 are 22.4 m/s, 20.8 m/s, and 18.2 m/s, respectively (these phase speeds were obtained by fitting a line to the zero θ anomaly shown in Fig. 15). Overall, the theoretical phase speeds are close to those observed in the dry simulations, further confirming that the column being disturbed is undergoing inertia-gravity oscillation.

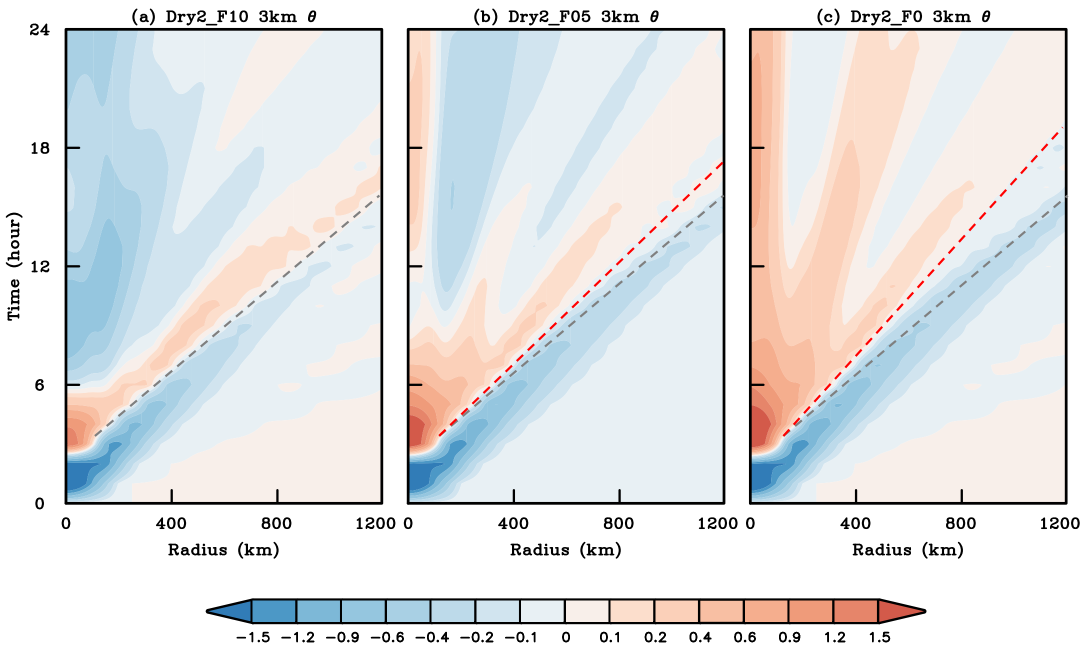

Fig. 15 Radius–time Hovmöller diagram of the azimuthal-mean of horizontal potential temperature anomaly (K) at 3 km height in (a) Dry2_F10, (b) Dry2_F05 and (c) Dry2_F0. The dashed black lines show the phase line where potential temperature anomaly changes sign in Dry2_F10, and the dashed red lines show those in Dry2_F05 and Dry2_F0, respectively.

Finally, we examine the response of the dry atmosphere to the first baroclinic heating mode, as this heating mode is also a dominant feature in tropical MCDs. The set of 'Dry1' simulations is designed similarly to the 'Dry2' simulations (Table 2), with the only difference being the application of the first baroclinic heating mode in the vertical direction (Fig. 4b). Upon model initialization, the deep heating triggers upward motion throughout the entire column (Figs. 16a-c). Although this upward motion induces adiabatic cooling, it is insufficient to counterbalance the diabatic heating, resulting in warming across the entire column during the first 2 hours (Figs. 16d-f). After the heating ceases, the upward motion continues, cooling and moistening the lower atmosphere. This free-tropospheric cooling and moistening would be expected to invigorate deep convection and prolong the presence of the first heating mode in full-physics simulations. After 6 hours, the vertical velocity becomes negative in the disturbance region (Figs. 16a-c), which reduces the cold and wet anomalies in the column (Figs. 16d-i). However, there is no clear recovery of upward motion or low-level buoyancy following this subsidence, so that any oscillation is sufficiently damped so as to exist for only one period. Furthermore, the magnitude of the response in the 'Dry1' simulations is significantly smaller than that of the 'Dry2' simulations. These results strongly suggest that it is the second baroclinic heating mode that is responsible for the inertia-gravity oscillation, especially in real-world scenarios.

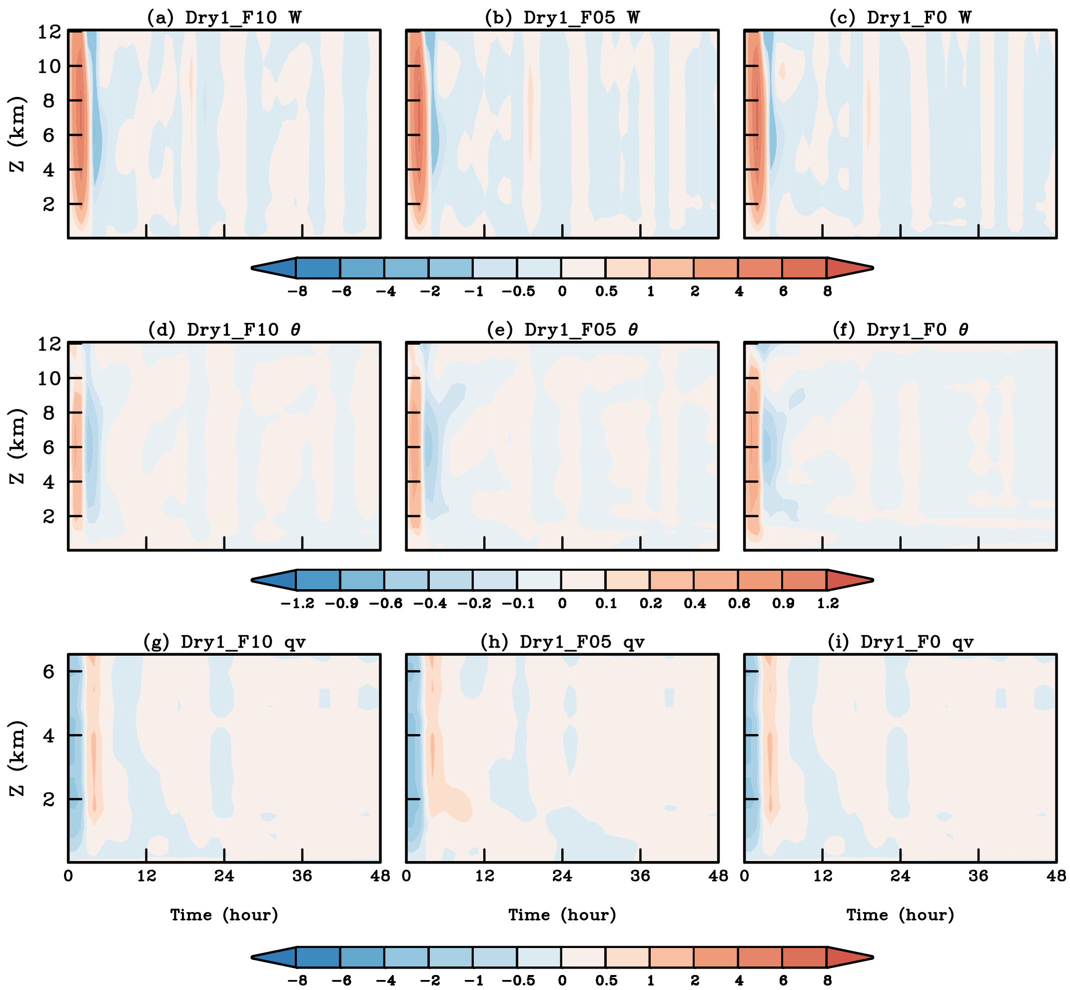

Fig. 16 As in Fig. 11, but for Dry1_F10, Dry1_F05 and Dry1_F0.

From the dry simulations in this section, we have demonstrated that in a background with rotation and stratification, an air column disturbed by mesoscale diabatic heatings can lead to oscillations, with the underlying mechanism being an inertial-gravity oscillation. In real-world scenarios, the stratiform heating profile plays a crucial role in the recovery of low-level buoyancy. Although the immediate response to the stratiform cooling in the lower free-troposphere does not favor low-level buoyancy recovery, the inertia-gravity oscillation triggered by the entire stratiform heating (vertical wavenumber 1) profile soon results in ascent at the lower levels of the disturbed air column. This upward motion cools and moistens the lower atmosphere, facilitating the recovery of low-level buoyancy and, consequently, initiating a new episode of deep convection.

During such oscillation of MCDs, the waves are internally excited by convection itself. Diabatic heating serves not only as a source for the subsequent oscillations of the air column but also as a consequence of the preceding oscillations. The wave source—namely, the convective heating—redevelops with each oscillation period, thereby establishing this phenomenon as a convectively coupled inertia-gravity oscillation. Although the oscillation of MCDs within convectively coupled inertia-gravity waves shown in previous studies (e.g., Heartel and Kiladis 2004; Kuang 2008) has also been termed a 'convectively coupled inertia-gravity oscillation', those oscillations are different from the one examined in this study. Those previous studies have primarily examined the influence of waves with characteristic scales of 2000-4000 km on convective activity in a region through which the waves horizontally propagate. To distinguish the phenomenon examined here from concepts presented in previous studies, we refer to the oscillation in this study as a "convectively coupled internal oscillation."

6. Discussion and Summary

Gravity waves serve as a crucial link between convective disturbances and their surrounding environments. On one hand, large-scale waves propagating across a region may produce quasi-periodic behavior of convection in that region by modifying the environmental conditions (e.g., Haertel and Kiladis 2004; Kuang 2008a; Kuang 2010; Tulich and Mapes 2010). On the other hand, latent heating within a convective disturbance can also initiate gravity waves that propagate away from the disturbance. While research on such convectively generated waves typically focuses on how these waves affect the remote environment—such as by radiating momentum and energy away from the disturbance (e.g., Bretherton and Smolarkiewicz 1989; Nicholls et al. 1991; Mapes 1993)—the influence of these waves on the subsequent behavior of the convective disturbance has received comparatively little attention. A useful analogy is that of a stone dropped into a calm pond: the disturbed water column not only generates gravity waves that propagate outward, but itself continues to oscillate after the initial disturbance.

In this study, we employ a series of idealized convective-permitting simulations to investigate the evolution of an atmospheric column being disturbed. Full-physics simulations demonstrate that the disturbed column typically exhibits internal damped oscillations in convective activity. Detailed analysis reveals that the oscillations in convection are primarily driven by oscillations in low-level buoyancy, which in turn arise from oscillations in temperature and moisture in the lower free-troposphere. By comparing dry simulations with linear gravity wave theory, we further show that the oscillations in lower-tropospheric temperature and moisture within the disturbed column are a consequence of inertia-gravity oscillations forced by an initial pulse of diabatic heating.

The convective oscillation seen in our research is internally generated, during which diabatic heating serves not only as a source for the subsequent inertia-gravity oscillations of the air column but also as a consequence of the preceding oscillations. Although inertia-gravity oscillations and convection can occur almost anywhere on Earth, we suggest that 'mesoscale' convective disturbances over 'tropical' oceans offer more favorable conditions for this oscillation to occur. Regarding disturbance size, a disturbance that is too small corresponds to a high frequency, which may be easily damped, while a disturbance too large tends to achieve a quasi-geostrophic balance, rendering convergence (and vertical velocity) negligible. Environmentally, the troposphere over tropical oceans has a relatively high background low-level buoyancy, so a small variation in low-level buoyancy there will lead to a larger variation in precipitation (Ahmed et al. 2020).

Two important points are highlighted from this research. The first is the critical role of low-level buoyancy in the life cycle of convective disturbances. In previous studies, latent heat release in convective disturbances is often linked to BL convergence. This concept has been incorporated into many cumulus parameterizations (e.g., Hayashi and Sumi 1986; Lau and Peng1987), but can lead to unphysical growth at the finest grid scales (sometimes termed the CISK catastrophe, e.g., Crum and Dunkerton 1992; Matthews and Lander 1999). Recent studies by Liu et al. (2019, 2022) proposed that latent heat release actually lags BL convergence, and cumulus parameterizations accounting for this time lag yield significantly better performance. Here we provide evidence that the variation of precipitation in a tropical MCD is not directly controlled by changes in the BL, but by variations in the lower-free tropospheric buoyancy. In our simulations, the time lag identified in Liu et al. (2019, 2022) would represent the time required for the system to transition from a low-level vertical velocity maximum to a temperature minimum, approximately one-fourth of the oscillation period (Fig. 8). Thus, recognizing the critical role of low-level buoyancy and its coupling with convection in inertia-gravity waves provides insights for improving cumulus parameterizations, especially for those based on the 'wave-CISK' perspective.

Our second important point concerns the critical role of stratiform heating in real-world tropical MCDs. Although stratiform heating initially leads to lower-tropospheric subsidence and a reduction in lower-tropospheric buoyancy, which does not favor convection, the subsequent phase of the oscillation results in upward motion and a recovery of buoyancy that triggers the next episode of convection. Compared to deep convective heating, stratiform heating is more effective in inducing oscillations. This sensitivity arises from the larger vertical wavenumber associated with stratiform heating, which results in slower outward propagation of energy, allowing more energy to remain available for maintaining the oscillation of the air column (e.g., Wu 2000; 2003). In real-world scenarios, stratiform heating is typically weaker than deep convective heating, making the internal oscillation susceptible to contamination and influence from other signals, such as large-scale waves and the diurnal cycle of insolation. Therefore, tropical MCDs with stronger intensity are more likely to exhibit an internal quasi-periodic oscillation. In a separate work, we will examine the role of this internal quasi-periodic oscillation in tropical cyclone precursors.

The internal oscillation identified in this work offers a new perspective for understanding and predicting the variations of observed tropical MCDs. The identification of this internal oscillation suggests that interactions between moist convectively coupled dynamics (in MCDs) and periodic forcings may be understood through the superposition of the internal mode with externally forced modes with differing amplitudes and periods. For example, the internal oscillation of an MCD that serves as a TC precursor could interact with the diurnal cycle of insolation, accelerating or delaying TC genesis depending on the phase of the superposition. To fully understand the internal oscillation, we need to identify the factors influencing the oscillation period. This study indicates that, in addition to the Coriolis parameter and stratification, a significant influence may arise from the coupling of convection. When coupled with convection, the recovery of low-level buoyancy occurs more swiftly than in dry cases, particularly when the Coriolis parameter is smaller (Figs. 5, 10b). This interplay of convection complicates the oscillation, necessitating further investigation.

Acknowledgement

We would like to thank Prof. David Neelin, Prof. Zhaohua Wu, Prof. Zhuo Wang, Dr. Yi-Hung Kuo and Prof. Hao Fu for useful discussions. This work is jointly supported by Beijing Natural Science Foundation JQ23037, the National Natural Science Foundation of China 42205004, the China Postdoctoral Science Foundation 2024T170011 and the China Scholarship Grant 202406010151. We thank the technical support of the National Large Scientific and Technological Infrastructure "Earth System Numerical Simulation Facility" (https://cstr.cn/31134.02.EL) and National Supercomputing Center in Wuzhen for computing resources.

Data availability statement.

All data and software for this paper are properly cited: the Jordan sounding found in Jordan (1958) and the WRF model found in Skamarock et al. (2019).

Appendix

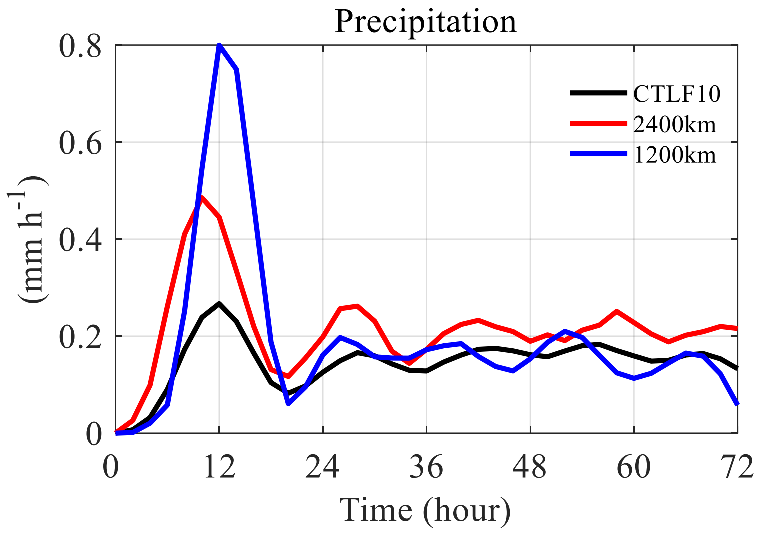

Fig. A1 Time series of precipitation (mm h^{-1}) averaged over the inner 150 km radii of the disturbance in full-physics simulations based on CTLF10 with different domain sizes.

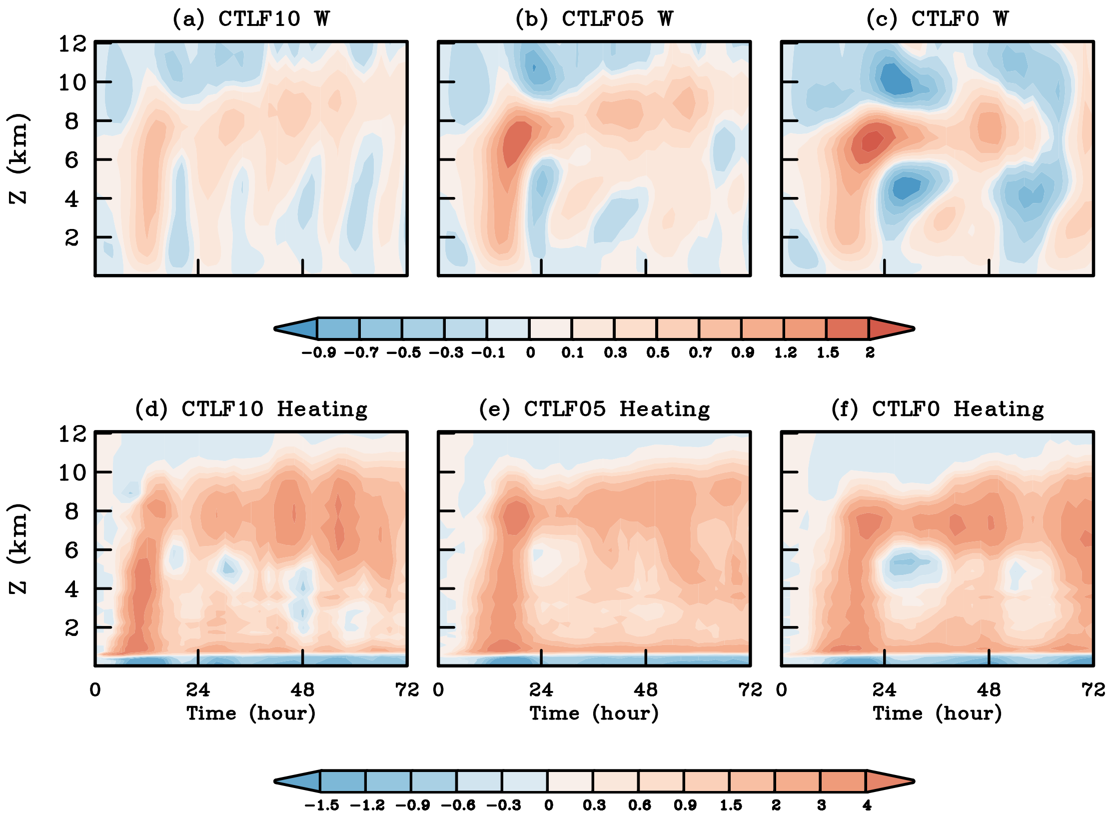

Fig. A2 Time-height plot of (a) vertical velocity ($\mathrm{cm\ s^{-1}}$) and (d) diabatic heating ($\mathrm{K\ day^{-1}}$), all averaged in the inner 150 km radii of the domain in CTLF10. (b) and (e) are the corresponding variables in CTLF05, and (c) and (f) are those in CTLF0, respectively.

Reference

1. Ahmed, F., and J. D. Neelin, 2018: Reverse engineering the tropical precipitation–buoyancy relationship. *J. Atmos. Sci.*, **75**, 1587-1608.
2. Ahmed, F., Á. F. Adames, and J. D. Neelin, 2020: Deep Convective Adjustment of Temperature and Moisture. *J. Atmos. Sci.*, **77**, 2163–2186.
3. Bretherton, C. S., and P. K. Smolarkiewicz, 1989: Gravity Waves, Compensating Subsidence and Detrainment around Cumulus Clouds. *J. Atmos. Sci.*, **46**, 740–759.
4. Browner, S. P., W. L. Woodley, and C. G. Griffith, 1977: Diurnal oscillation of the area of cloudiness associated with tropical storms. *Mon. Wea. Rev.*, **105(7)**, 856–864.
5. Crum, F. X., and T. J. Dunkerton, 1992: Analytic and numerical models of wave–CISK with conditional heating. *J. Atmos. Sci.*, **49**, 1693–1708.
6. Diaz, M., and W. R. Boos, 2021a: Evolution of idealized vortices in monsoon-like shears: Application to monsoon depressions. *J. Atmos. Sci.*, **78**, 1207–1225.
7. Diaz, M., and W. R. Boos, 2021b: The influence of surface heat fluxes on the growth of idealized monsoon depressions. *J. Atmos. Sci.*, **78**, 2013–2027.
8. Dunion, J. P., C. D. Thorncroft, and C. S. Velden, 2014: The Tropical Cyclone Diurnal Cycle of Mature Hurricanes. *Mon. Wea. Rev.*, **142**, 3900–3919.
9. Emanuel, K., 2018: 100 years of progress in tropical cyclone research. *Meteorol. Monogr.*, **59**, 11–15.
10. Fingerhut, W. A., 1978: A Numerical Model of a Diurnally Varying Tropical Cloud Cluster Disturbance. *Mon. Wea. Rev.*, **106**, 255–264.
11. Gray, W. M., and R. W. Jacobson Jr., 1977: Diurnal variation of deep cumulus convection. *Mon. Wea. Rev.*, **105**, 1171–1188.
12. Haertel, P. T., and R. H. Johnson, 1998: Two-day disturbances in the equatorial western Pacific. *Quart. J. Roy. Meteor. Soc.*, **124**, 615 636.
13. Haertel, P. T., and G.N. Kiladis, 2004: Dynamics of 2-day equatorial waves. *J. Atmos. Sci.*, **61**, 2707–2721.
14. Hayashi, Y., and A. Sumi, 1986: The 30–40 day oscillations simulated in an ‘‘aqua-

planet" model. *J. Meteor. Soc. Japan*, **64**, 451–467.

15. Holton, B. J. R. and G. J. Hakim, 2012: An Introduction to Dynamic Meteorology. 5th ed. Academic Press, 535 pp.
16. Hong, S. Y., Y. Noh, and J. Dudhia, 2006: A new vertical diffusion package with an explicit treatment of entrainment processes. *Mon. Wea. Rev.*, **134**, 2318–234.
17. Houze, R. A., 1982: Cloud clusters and large-scale vertical motions in the tropics. J. Meteor. Soc. Japan, 60, 396–410
18. Houze, R. A., 2018: 100 Years of Research on Mesoscale Convective Systems. *Meteor. Monogr.*, **59**, 17.1–17.54.
19. Iacono, M. J., J. S. Delamere, E. J. Mlawer, M. W. Shephard, S. A. Clough, and W. D. Collins, 2008: Radiative forcing by long-lived greenhouse gases: Calculations with the AER radiative transfer models. *J. Geophys. Res*., **113**, D13103.
20. Jordan, C. L., 1958: Mean soundings for the West Indies area. *J. Meteor.*, **15**, 91–97.
21. Klemp, J. B., and D. K. Lilly, 1978: Numerical simulation of hydrostatic mountain waves, *J. Atmos. Sci.*, **35**, 78–107.
22. Kuang, Z., 2008: A moisture-stratiform instability for convectively coupled waves. *J. Atmos. Sci.*, **65**, 834–854.
23. Kuang, Z., 2010: Linear Response Functions of a Cumulus Ensemble to Temperature and Moisture Perturbations and Implications for the Dynamics of Convectively Coupled Waves. *J. Atmos. Sci.*, **67**, 941–962.
24. Lau, K., and L. Peng, 1987: Origin of Low-Frequency (Intraseasonal) Oscillations in the Tropical Atmosphere. Part I: Basic Theory. *J. Atmos. Sci.*, **44**, 950–972
25. Li, T., X. Ge and B. Wang, 2006: Tropical cyclogenesis associated with Rossby wave energy dispersion of a preexisting typhoon. Part II: Numerical simulations. *J. Atmos. Sci.*, **63**, 1390–1409.
26. Liu, Y., Z. Tan, and Z. Wu, 2019: Noninstantaneous wave-CISK for the interaction between convective heating and low-level moisture convergence in the tropics. J. *Atmos. Sci.*, **76**, 2083–2101.

27. Liu, Y., Z. Tan, and Z. Wu, 2022: Convective Response in a Cloud-Permitting Simulation of the MJO: Time Scales and Processes. *J. Atmos. Sci.*, **79**, 1473–1490.

28. Matthews, A. J., and J. Lander, 1999: Physical and numerical contributions to the structure of Kelvin wave-CISK modes in a spectral transform model. *J. Atmos. Sci.*, **56**, 4050–4058.

29. Mapes, B. E., 1993: Gregarious Tropical Convection. *J. Atmos. Sci.*, **50**, 2026–2037.

30. Mapes, B. E., 2000: Convective inhibition, subgrid-scale triggering energy, and stratiform instability in a toy tropical wave model. *J. Atmos. Sci.*, **57**, 1515–1535.

31. Nesbitt, S. W., E. J. Zipser, and D. J. Cecil, 2000: A census of precipitation features in the tropics using TRMM: Radar, ice scattering, and lightning observations. *J. Climate*, **13**, 4087-4106.

32. Nicholls, M. E., R. A. Pielke, and W. R. Cotton, 1991: Thermally Forced Gravity Waves in an Atmosphere at Rest. *J. Atmos. Sci.*, **48**, 1869–1884.

33. Nicholls, M. E., and M. Montgomery, 2013: An examination of two pathways to tropical cyclogenesis occurring in idealized simulations with a cloud-resolving numerical model. *Atmos. Chem. Phys.*, **13**, 5999–6022.

34. Nicholls, M. E., 2015: An investigation of how radiation may cause accelerated rates of tropical cyclogenesis and diurnal cycles of convective activity. *Atmos. Chem. Phys.*, **15**, 9003–9029.

35. Nolan, D. S., 2007: What is the trigger for tropical cyclogenesis? *Aust. Meteor. Mag.*, **56**, 241–266.

36. Skamarock, W. C., Klemp, J. B., Dudhia, J., Gill, D. O., Liu, Z., Berner, J., Wang, W., Powers, J. G., Duda, M. G., Barker, D. M., and Huang, X.-Y. (2019), A Description of the Advanced Research WRF Model Version 4, UCAR/NCAR, https://doi.org/10.5065/1DFH-6P97.

37. Takayabu, Y. N., 1994: Large-scale cloud disturbances associated with equa torial waves. Part II: Westward-propagating inertio-gravity waves. *J. Meteor. Soc. Japan*, **72**, 451–465.

38. Takayabu, Y. N., K. M. Lau, and C. H. Sui, 1996: Observation of a quasi-2-day

wave during TOGA COARE. *Mon. Wea. Rev.*, **124**, 1892–1913.

39. Thompson, G., R. M. Rasmussen, and K. Manning, 2004: Explicit forecasts of winter precipitation using an improved bulk microphysics scheme. Part I: Description and sensitivity analysis. *Mon. Wea. Rev.*, **132**, 519–542.
40. Tulich, S. N., and B. E. Mapes, 2010: Transient environmental sensitivities of explicitly simulated tropical convection. *J. Atmos. Sci.*, **67**, 923–940.
41. Wheeler, M., and G. N. Kiladis, and P. J. Webster, 2000: Large-scale dynamical fields associated with convectively coupled equatorial waves. *J. Atmos. Sci.*, **57**, 613–639.
42. Wu, Q., Ruan, Z., Chen, D. and Lian, T., 2015: Diurnal variations of tropical cyclone precipitation in the inner and outer rainbands. *J. Geophys. Res.*, **120**, 1–11.
43. Wu, Z., E. S. Sarachik, and D. S. Battisti, 2000b: Vertical structure of convective heating and the three-dimensional structure of the forced circulation on an equatorial beta plane. *J. Atmos. Sci.*, **57**, 2169–2187.
44. Wu, Z., 2003: A shallow CISK, deep equilibrium mechanism for the interaction between large-scale convection and large-scale circulations in the tropics. *J. Atmos. Sci.*, **60**, 377–392.
45. Yang, B., and Z.-M. Tan, 2020: Interactive radiation accelerates the intensification of the midlevel vortex for tropical cyclogenesis. *J. Atmos. Sci.*, **77**, 4051–4065.